http://dx.doi.org/10.1016/j.ijheatmasstransfer.2019.01.072

Study on the mixed dynamic recrystallization mechanism of Inconel 740 superalloy during hot deformation

M. J. Wang[a,b], C. Y. Sun[a,b,*], M.W. Fu[c,#] , Z. L. Liu[d], L. Y. Qian[a,b]

[a] School of Mechanical Engineering, University of Science and Technology Beijing, Beijing, 100083, China

[b] Beijing Key Laboratory of Lightweight Metal Forming, Beijing, 100083, China

[c] Department of Mechanical Engineering, The Hong Kong Polytechnic University, Hung Hom, Kowloon, Hong Kong, China

[d] School of Nuclear Equipment and Nuclear Engineering, Yantai University, Yantai, 264005, China

Abstract

The dynamic recrystallization (DRX) mechanisms of Inconel 740 superalloy were studied by the electron backscatter diffraction (EBSD) analyses of the superalloy microstructures obtained under different deformation conditions. The results show that the discontinuous dynamic recrystallization (DDRX) occurs together with the continuous dynamic recrystallization (CDRX), but CDRX plays a minor role during hot deformation. CDRX easily happens at the low deformation temperature (1000 ˚C), high strain rate (1.0 s^{-1}) and medium strain (0.51). A mixed DRX mechanism is proposed to facilitate the occurrence of DRX, which in turn consists of DDRX covering the pre-existing grain boundary bulging and the twinning assisting nucleation, and CDRX involving the progressive rotation of subgrain near the pre-existing grain boundaries and the homogeneous misorientation increase within the deformed grain interiors. The mixed DRX mechanism is validated via the observation of process of DRX and helps establish an in-depth understanding and insights into DRX occurrence, behavior and mechanism of Inconel 740 superalloy in such a way to facilitate configuring and controlling the needed microstructure, and tailoring the required properties of the products made of Inconel 740 superalloy via hot forming process.

Keywords: Dynamic recrystallization; Twinning; Misorientation; Inconel 740 superalloy

Corresponding authors:

* C. Y. Sun: Tel.: +86-10-62332261, E-mail: suncy@ustb.edu.cn (C. Y. Sun).

M.W. Fu: Tel.:852-27665572, Email: mmmwfu@polyu.edu.hk (M. W. Fu).

1. Introduction

Inconel 740 superalloy with the unique performance is expected to be a promising superheater and reheater material for advanced ultra-supercritical steam boiler unit [1, 2]. To promote its wide application in industries, huge efforts have been provided to study its oxidation behavior [3], thermal stability [4], creep behavior [5, 6] and new smelting method [7]. The DRX behavior of Inconel 740 superalloy during hot forming process, however, has not yet been systematically studied. This behavior is an important factor which affects the industrial application of this superalloy. Usually, DRX not only reduces the thermal deformation resistance and refines the original coarse grain size of the metallic materials, but also improves the mechanical properties of the deformed parts [8, 9]. Therefore, an in-depth understanding of DRX mechanism of Inconel 740 alloy is critical.

Compared with dynamic recovery (DRV), it is well known that dynamic recrystallization (DRX) is a predominant softening mechanism in Nickel-based superalloys with the low stacking fault energy (SFE). The conventional discontinuous dynamic recrystallization (DDRX) characterized with the local bulge of grain boundaries is the main nucleation mechanism in Nickel-based superalloys. This mechanism is enhanced by the increase of deformation temperature and the decrease of strain rate [10-12]. Furthermore, by accelerating the bulge of original boundaries and the subsequent bulge separation from the remaining boundaries, twinning can promote the nucleation and growth of recrystallized grains for Nickel-based superalloys [13, 14]. On the other hand, the continuous dynamic recrystallization (CDRX) featured by the progressive rotation of subgrain have been also found in the past few years in other Nickel-based superalloys [15-20], despite of the fact that CDRX is considered to be prone to occur in metallic materials with high SFE [21]. A number of researchers have conducted an investigation into this issue. Zhang et al. [16] demonstrated that CDRX occurred at a smaller strain (0.3) and low deformation temperature. Lin et al. [19] considered that CDRX was developed at a medium strain (0.52), and was slightly susceptive to the variation of deformation temperature and strain rate. Azarbarmas et al. [20] revealed that CDRX can be facilitated to occur at the low temperature and high strain rate. Therefore, the favorable deformation conditions for the occurrence of CDRX in Nickel-based superalloys have not yet reached a consensus. To explore more on CDRX, the electron backscattered diffraction (EBSD) is a most important technology employed to identify and reveal DRX mechanisms in the above researches, which have demonstrated that DDRX and

CDRX tend to occur simultaneously. However, in-depth researches need to be done to illustrate the effect of different deformation conditions, i.e., the variation of strain (ε), strain rate ($\dot{\varepsilon}$) and temperature (T), on the DRX mechanism, especially for an in-depth understanding of CDRX and insight into its mechanism.

In this research, DRX behavior was investigated by a series of isothermal compression experiments and the research focus was more on DRX mechanism by using Inconel 740 superalloy as the testing material. The typical microstructures involved in different DRX mechanisms and corresponding local misorientations were thoroughly explored and discussed. The deformation conditions in which CDRX was prone to take place were identified by the quantitative analysis of misorientation angle change. The research thus provides a basis for designing the needed microstructure and controlling the required properties of this unique and promising superalloy.

2. Material and methods

The nominal chemical compositions (*wt*.%) of Inconel 740 superalloy are 0.03C-0.5Mo-0.5Si-0.3Mn-20Co-0.9Al-25Cr-0.7Fe-1.8Ti-2.0Nb and (Bal.) Ni. The specimens of φ 8×12mm were taken from a forged billet. These cylindrical specimens were solution treatment at 1150 ˚C for 30 min, and then were water-cooled to ensure a single phase structure to be obtained. Two experimental plans were designed through considering the influences of different deformation temperatures and strain rates on the microstructures of the superalloy. The first one is that the specimens were deformed at an invariable strain rate (0.01 s^{-1}), three deformation temperatures (1000, 1100 and 1200 ˚C) and four true strains (0.22, 0.36, 0.51 and 0.8). Those specimens in the second one were compressed at a constant temperature (1100 ˚C), two strain rates (0.1 and 1.0 s^{-1}) and four strains (0.22, 0.36, 0.51 and 0.8). The second one combined the temperature condition of 1100 ˚C in the first plan, considering conjointly the influence of different strain rates on the microstructure of the superalloy. Moreover, the effect of the true strain on DRX mechanism was also studied based on the above two plans. The compression experiments of the two plans were performed in Gleeble-3500 thermal simulator. The tantalum foils were used as lubricant and put between the end faces of specimens and the dies of simulator for reducing friction. Before loading, the specimens was heated at a heating rate of 5 ˚C/s to the testing temperature, and subsequently soaked for 180s to insure the uniform temperature distribution in the specimen. Upon the

completion of the compressive tests, all the specimens were instantly water-quenched to maintain the high temperature microstructure.

These compressed specimens were then sectioned longitudinally for analysis of their microstructures. The observation location was in the central region of above section. The observation surfaces of the specimens were ground and polished mechanically. For optical microscope examination, the observation surfaces were etched for 15 s in the aqua regia solution. For EBSD analysis, the observation surfaces were electropolished for 10s in a mixture of 40 ml vitriol and 160 ml methyl alcohol at the room temperature. The given step size of 0.8 and 3.2 μm in EBSD were performed for scanning the deformed microstructure and initial microstructure, respectively. The scanned data were processed subsequently by Channel 5 software. Furthermore, the low angle grain boundaries (LAGBs, $3°<\theta<10°$), the medium angle grain boundaries (MAGBs, $10°<\theta<15°$) and the high angle grain boundaries (HAGBs, $\theta>15°$) were unequivocal on the basis of the misorientation angle (θ) of adjacent grains. Band contrast maps attaching LAGBs, MAGBs and HAGBs were used for displaying the deformed microstructure.

3. Results and discussion

3.1. Initial microstructure

The specimen after solution treatment and before hot deformation is regarded as the initial state of Inconel 740 superalloy. Fig.1 (a) shows the microstructure consisted of annealing twins and equiaxed grains, which indicates the static recrystallization structure of initial material [20]. The initial microstructure appears to be free of any other phase, therefore, is considered as a single phase matrix. The distribution of initial misorientation angle is inclined absolutely towards HAGBs. Fig. 1 (b) shows that the fractions of LAGBs, MAGBs and HAGBs are evaluated as 0.9%, 0.6% and 98.5%, respectively.

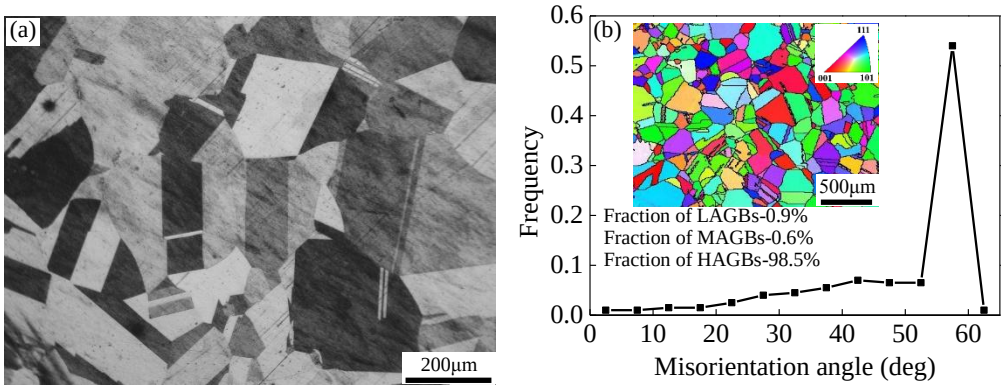

Fig.1. Initial state of Inconel 740 superalloy: (a) optical microscope and (b) distribution of misorientation angle.

3.2. Determination of critical strain

The flow curves can be categorized as two kinds of DRV and DRX. The stress values of dashed lines in Fig.2 (a) correspond with the steady-state stress (σ_{ss}) and the saturation stress (σ_{sat}) achieved by DRX and DRV softening mechanisms, respectively. The values of σ_{sat} and σ_{ss} are acquired by the curve of stress (σ) and work hardening rate ($\theta=d\sigma/d\varepsilon$) [22, 23], as shown in the small diagram of Fig.2 (a). σ_{sat} is determined as a σ value, which is the abscissa of intersection of dashed line (θ=0) and tangent line through the inflection point on θ-σ curve. σ_{ss} is consistent with the intersection abscissa of dashed line (θ=0) and rising θ-σ curve. Therefore, according to the type of the flow curve acquired at 0.01 s^{-1} and 1200 ˚C, DRX can be as a main softening mechanism for Inconel 740 superalloy. Moreover, the small diagram in Fig. 2 (a) depicts the abscissa of inflection point, i.e., the critical stress (σ_c) of DRX initiation [23]. The critical strain (ε_c) of initiating DRX is determined correspondingly based on the σ_c value in the true stress-strain curve. Consequently, ε_c values of Inconel 740 superalloy under the deformation conditions of deformation temperatures of 1000, 1100 and 1200 ˚C and strain rates of 0.01, 0.1 and 1.0 s^{-1} are displayed in Fig. 2 (b). The above deformation conditions were applied to the previous research [24] and they included the deformation conditions involving the strain of 0.8 in this study. The used true strains in this study are always larger than ε_c to ascertain the occurrence of DRX.

The appearance of peak strain (ε_p) on the flow curve usually confirms the occurrence of DRX in metallic material, while DRX behavior is assuredly activated earlier than ε_p [23]. ε_p is corresponding to the peak stress (σ_p), as shown in Fig. 2 (a). ε_c is usually defined as a linear

function associated with ε_p, i.e., $\varepsilon_c=C\varepsilon_p$. In order to be more statistical, using the above deformation conditions [24], the slope (C) is evaluated by the linear fitting of ε_c and ε_p obtained at different deformation conditions. Therefore, the function relationship of ε_c and ε_p of Inconel 740 superalloy can be expressed as $\varepsilon_c=0.6\varepsilon_p$.

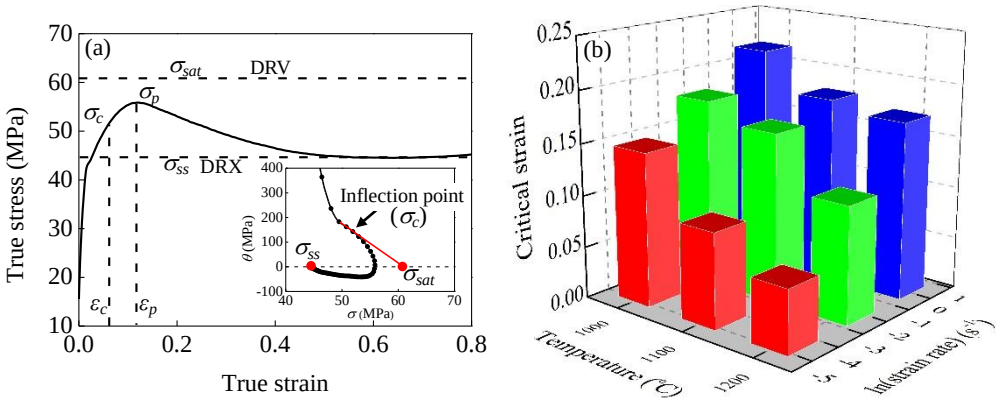

Fig.2. DRX behavior of Inconel 740 superalloy: (a) flow curve and a relationship between θ and σ obtained at T=1200 ˚C and $\dot{\varepsilon}$=0.01 s^{-1}; (b) ε_c values at different deformation conditions.

3.3. Characteristic deformed microstructure

The impact of different deformation temperatures on the microstructures obtained at the strain rate of 0.01 s^{-1} and strain of 0.51 is exhibited in Fig. 3. The black, blue and red lines represent HAGBs, MAGBs and LAGBs, respectively. The color code of all the following band contrast maps is the same as Fig. 3. It is clear that the size and volume fraction of DRX grains are obviously affected by the change of deformation temperatures. Fig. 3 (a) represents some small DRX grains located at the initial grain boundaries and triple junctions at 1000 ˚C. Moreover, a mass of LAGBs are detectable within the initial grains, especially, near the serrated and bulging pre-existing HAGBs. These LAGBs is connection with the dislocation substructures induced by DRV [19, 25, 26]. As the deformation temperature is increased to 1100 ˚C, as illustrated in Fig. 3 (b), the more and bigger DRX grains are appeared. Furthermore, the microstructure is consisted of equiaxed and homogeneous DRX grains at 1200 ˚C, as indicated in Fig. 3 (c). In generally, DRX behavior is thermally activated process. From Fig.2 (b), the higher deformation temperature results in less ε_c. The accumulation and interaction of dislocations at the high deformation temperature lead to the more DRX grain nuclei [26]. Meanwhile, a high deformation temperature also provides a sufficient driving force required for the grain boundary migration. Therefore, by means of high temperature, the

increase in both rates of DRX grain nucleation and grain boundary migration promotes DRX process.

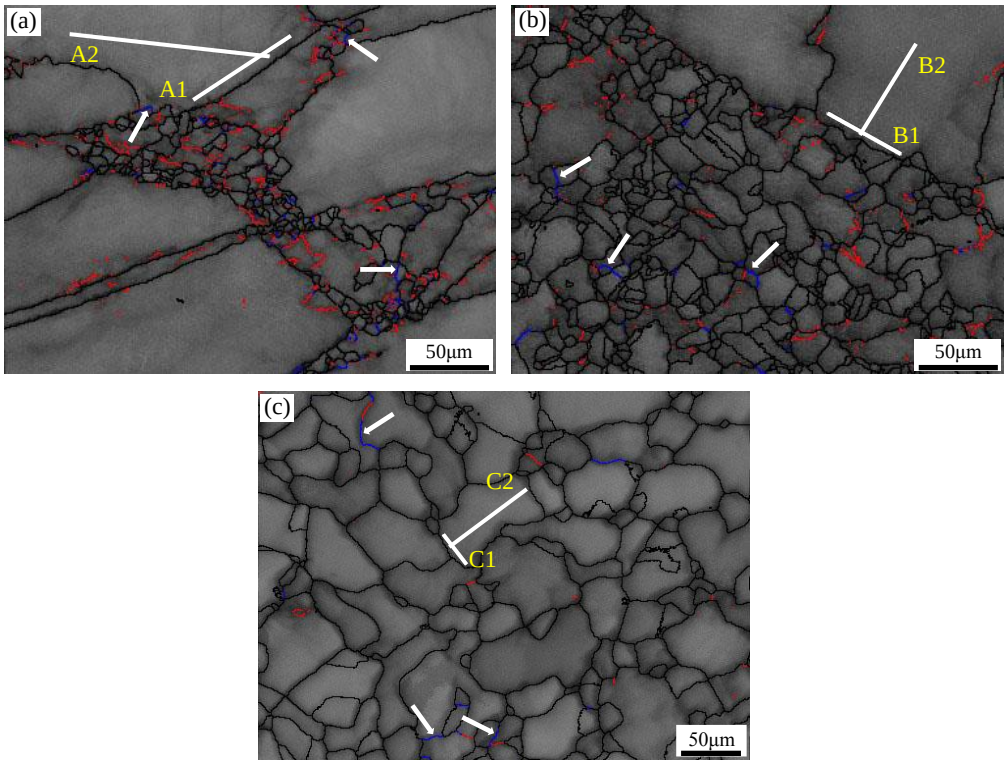

Fig.3. The microstructure of Inconel 740 superalloy obtained at ε=0.51 and $\dot{\varepsilon}$=0.01 s^{-1} with a deformation temperature of: (a) 1000 ˚C; (b) 1100 ˚C and (c) 1200 ˚C. (color code: black-HAGBs, blue-MAGBs and red-LAGBs).

The strain rate is considered as the other important factor for affecting DRX behavior. The effect of different strain rates on the microstructures obtained at the temperature of 1100 ˚C and strain of 0.8 is illustrated in Fig. 4. The completed recrystallization microstructure composed of bigger DRX grains is acquired at 0.01 s^{-1}. With the strain rate increasing to 0.1 s^{-1}, as shown in Fig. 4(b), the partial DRX microstructure with the smaller DRX grains is clearly observed. Fig. 4 (c) shows that the microstructure is made up of some much finer DRX grains and initial deformed grains as the strain rate is further increased to 1.0 s^{-1}. These fine DRX grains are in the form of the typical necklace structure along the original HAGBs. Therefore, DRX degree corresponding to the volume fraction and size of DRX grains, is significantly decreased with the increase of strain rate. From Fig.2 (b), ε_c is visibly increased as the strain rate is increased. By comparing Figs. 4 (b) and (c), the more LAGBs are seen inside the deformed grain interiors and near initial HAGBs under a high strain rate condition.

These LAGBs are also generated by the dislocation accumulation and rearrangement. In other words, the higher strain rate provides more nucleation sites used for DRX grain nuclei. However, the inadequate deformation time due to the high strain rate inhibits the growth of DRX grain nucleus. As a result, the higher strain rate leads to the finer DRX grains and the lower DRX fraction in microstructure.

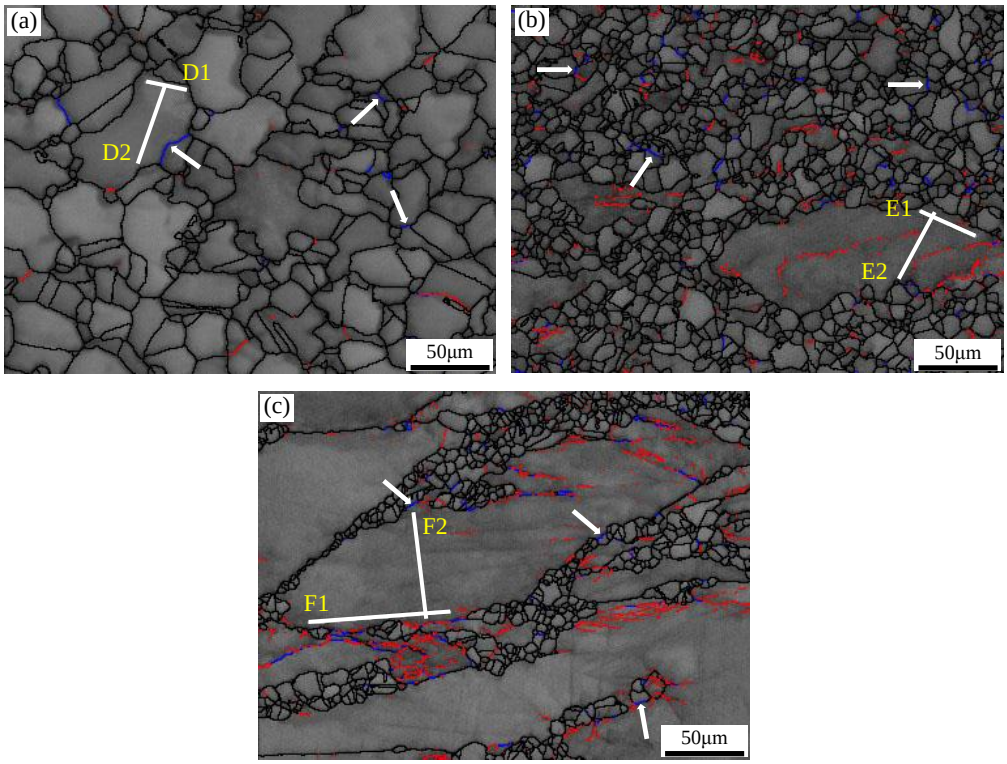

Fig.4. The microstructure of Inconel 740 superalloy obtained at ε=0.8 and T=1100 ˚C with a strain rate of: (a) 0.01 s^{-1}; (b) 0.1 s^{-1} and (c) 1.0 s^{-1}.

The bulging of pre-existing grain boundaries and the necklace structures are observed in Figs. 3 (a) and 4(c). Such a morphology of microstructures indicates DRX grain nucleation falling into DDRX mechanism. Furthermore, MAGB is regarded to be a transition stage from LAGB to HAGB and its presence is necessary for CDRX mechanism characterized by the progressive subgrain rotation [27, 28]. The transition stage, i.e., blue MAGBs presented by the white arrows in Figs. 3 and 4, is obvious. Therefore, during hot deformation of Inconel 740 superalloy, DDRX and CDRX mechanisms concurrently occur. Both DRX mechanisms are analyzed deeply in subsequent section.

3.4. Variation of misorientation angle

The analyses of misorientation gradients influenced by different deformation temperatures and strain rates are realized by the point to point (local) and point to origin (cumulative) misorientations, as shown in Fig. 5. Here the relative difference in the crystal orientation between two neighbor scanning points is defined as the local misorientation and that between two non-adjacent ones is defined as the cumulative misorientation [29]. From Fig. 5, the black and red lines represent the local and cumulative misorientations, respectively. The position of misorientation angle 10° is given by the blue dotted line. The white lines used for measuring the misorientation gradients along the grain boundary (#1) and across the elongated or coarser grain interior (#2) are marked in Figs. 3 and 4, respectively. A grain boundary with a misorientation angle between 10 and 15°, belongs to MAGB which is connected with the process of subgrain evolution, and also is needed for nucleation of DRX grains in CDRX [20, 27]. Figs. 5 (a) and (b) illustrate that both the cumulative misorientations near the grain boundary and inside the grain exceed 10° at 1000 ˚C. It is demonstrated that the progressive rotation of subgrain caused by the misorientation accumulation is well developed along the grain boundaries and inside the grains [14]. As the temperature is increased, the cumulative misorientations are decreased gradually in Figs. 5 (c)-(f). Such a phenomenon means that the influence of sub-boundary evolution involved in CDRX becomes weak gradually. The local misorientations (less than 1.5°) do not change much in the process of increasing deformation temperature. By comparing Figs. 5 (a)-(f), it is sure that the role of CDRX mechanism is getting less and less effective with the increase of temperature. Furthermore, Figs. 5 (g)-(l) reveal the misorientation gradients influenced by the increasing strain rate. From Figs. 5 (g)-(h), the cumulative misorientations are very low at 0.01 s^{-1}. The misorientation angles in Figs. 5 (i)-(j) exceed readily 10° with the strain rate increasing to 0.1 s^{-1}. Specially, the misorientation angles surpass more than 20° at 1.0 s^{-1}, as indicated in Figs. 5 (k)-(l). The sharp increase of misorientation angle implies that the misorientations along the grain boundaries and within the grains are accumulated adequately at the high strain rate. The large misorientation gradient derived by misorientation accumulation provides an adequate misorientation to turn LAGBs into HAGBs in CDRX mechanism. Therefore, the role of CDRX is strengthened with the increase of strain rate. Furthermore, the increase of strain rate does not significantly affect the local misorientations (less than 1.9°) in Figs. 5 (g)-(l).

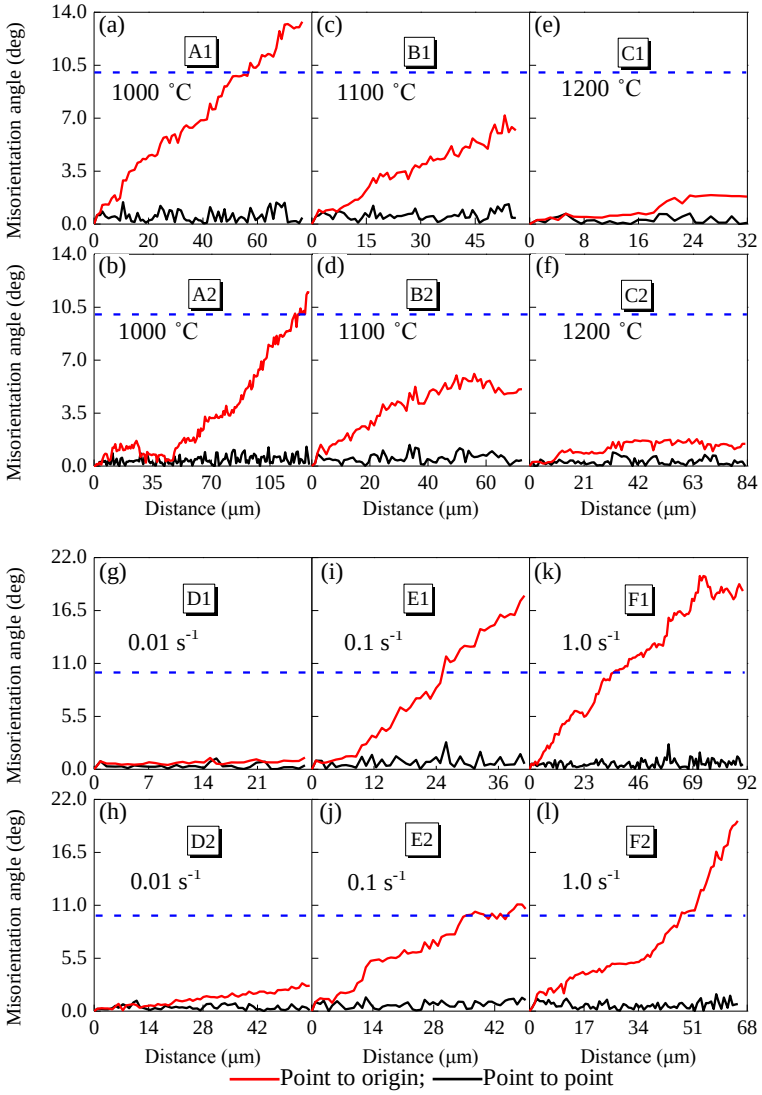

Fig.5. Variations of misorientation gradient measured along A-F lines marked in Figs. 3 and 4.

Fig. 6 plots the distribution of misorientation angles obtained under different deformation conditions. The average misorientation angle (θ_{Ave}) presented in Fig. 6 (a) is increased from 36.8° to 42.7° with the temperature increasing from 1000 to 1200 ˚C. Fig. 6 (c) shows that θ_{Ave} is decreased from 44.3° to 36.1° when the strain rate is increased from 0.01 to 1.0 s^{-1}. θ_{Ave} is increased from 29.3° to 40.9° as the strain is increased from 0.22 to 0.8, as indicated in Fig. 6 (e). The evolution characteristic of θ_{Ave} is in connection with the DRX grain growth and volume fraction, i.e., DRX behavior kinetics [10, 30]. Therefore, if the deformation conditions more favor DRX occurrence, θ_{Ave} is larger. Moreover, the dashed curves in Figs. 6 (a), (c) and (e) are plotted as Mackenzie distribution, which means the probability distribution of misorientation angle in the cubic polycrystalline materials [31]. θ_{Ave} is always smaller than

peak value (obtained at 45°) of Mackenzie distribution. This is because that LAGBs can be introduced all the time during hot deformation due to the dynamically evolved characteristic of grain structure [32].

In addition, the fractions of LAGBs, MAGBs and HAGBs are given for an in-depth insight into the grain boundary characteristics involved in DDRX and CDRX mechanisms, as illustrated in Figs. 6 (b), (d) and (f). Figs. 6 (b), (d) and (f) are corresponded with those deformation conditions in Figs. 6 (a), (c) and (e), respectively. Fig. 6 (b) describes that the fraction of LAGBs is rapidly decreased with the increase of temperature, whereas that of HAGBs is a reversed tendency. It is owing to the development of DRX grains with dislocation-free with the increase of deformation temperature, as indicated in Fig. 3. A mass of LAGBs formed through the dislocation rearrangement are eliminated by HAGBs migration of DRX grains. Moreover, the role of CDRX can be enhanced through the increase in fraction of MAGBs [28, 33]. The fraction of MAGBs is decreased from 3.1% to 1.6% when the temperature is increased from 1000 to 1200 ˚C, as shown in Fig. 6 (b), indicating the weak role of CDRX at the high deformation temperature. Fig. 6 (d) illustrates that the fraction of HAGBs is decreased with the strain rate increasing, while that of LAGBs is increased quickly. The dislocation interaction is strengthened at the high strain rate [33], leading to a lot of LAGBs networks (Fig. 4 (c)) formed by dislocation substructures within the deformed grain interior and near HAGBs. Fig. 6 (d) also reveals that when the strain rate is increased from 0.01 to 1.0 s^{-1}, the fraction of MAGBs is increased from 1.5% to 3.6%. Therefore, the effect of subgrain evolution involved in CDRX is promoted by the high strain rate. Moreover, the fractions of LAGBs, MAGBs and HAGBs with the change of strain are depicted in Fig. 6 (f).When the strain is less than 0.36, the fraction of LAGBs is increased continuously to 34.5%, which is much larger than the initial state. This indicates that the accumulation of dislocation results in the generation of plentiful LAGBs at the early to middle deformation. With the further increase of strain, the development of DRX grains with dislocation-free causes the decrease in the fraction of LAGBs. The fraction of HAGBs is also inversely proportional to that of LAGBs in the process of increasing strain. It is noteworthy that the fraction of MAGBs is increased from 0.6% at the initial state to 5.7% at the strain of 0.51, which implies that the subgrain evolution in CDRX is more active at the medium strain. Nevertheless, when the strain is greater than 0.51, the fraction of MAGBs is reduced due to the well development of DRX grains with dislocation-free in Fig. 4 (b).

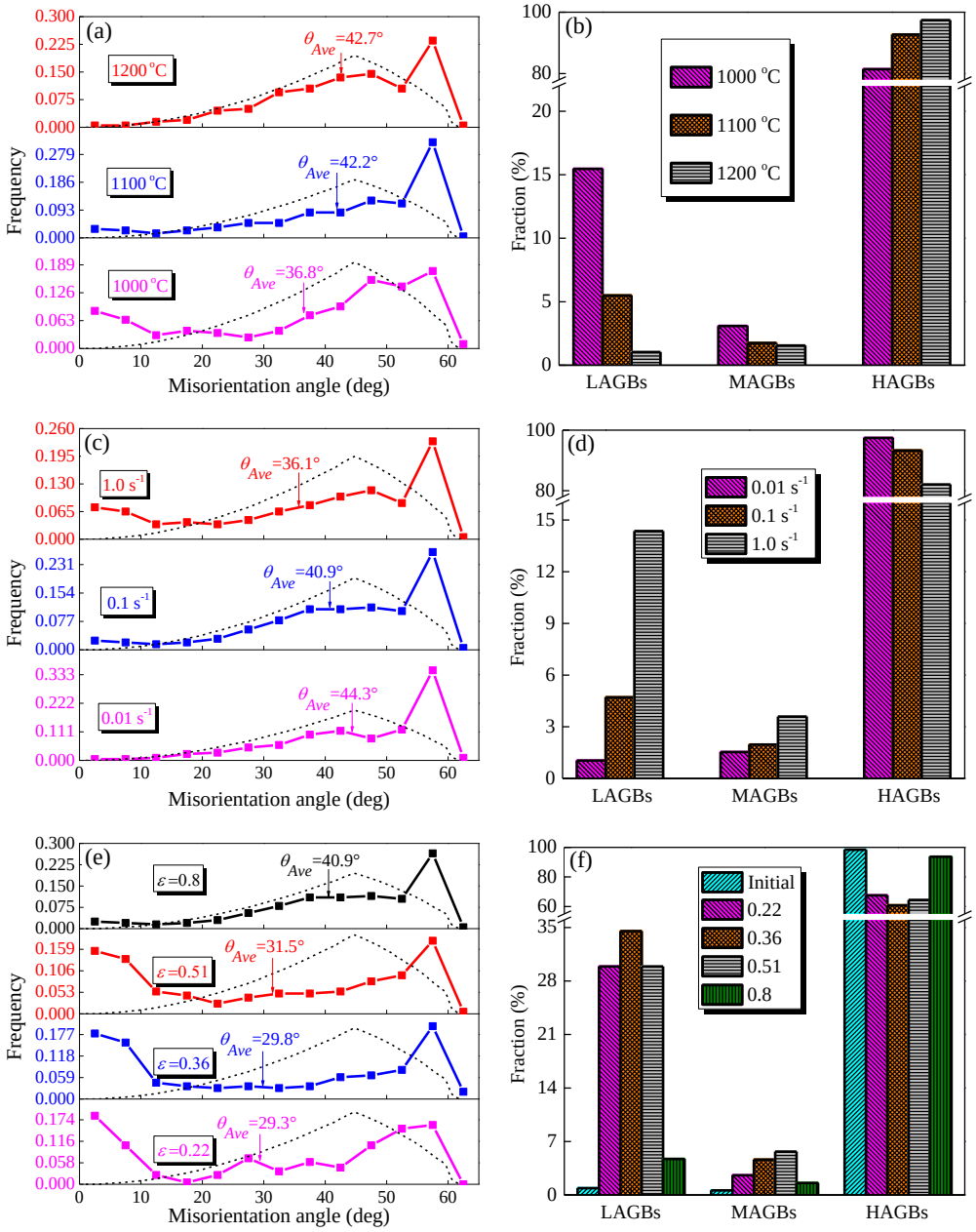

Fig.6. Distributions of misorientation angle of Inconel 740 superalloy obtained at: (a) at $\dot{\varepsilon}$ =0.01 s^{-1} and ε=0.51 with different deformation temperatures of 1000, 1100 and 1200 ˚C; (c) T=1100 ˚C and ε=0.8 with different strain rates of 0.01, 0.1 and 1.0 s^{-1}; (e) T=1100 ˚C and $\dot{\varepsilon}$ =0.1 s^{-1} with different true strains of 0.22, 0.36, 0.51 and 0.8. (b), (d) and (f) corresponding to the fractions of LAGBs, MAGBs and HAGBs in (a), (c) and (e), respectively.

As a brief summary, during hot deformation of Inconel 740 superalloy, both DDRX and CDRX mechanisms take place simultaneously (Section 3.3). The analyses of misorientation gradient (Fig. 5) and fraction of MAGBs (Figs. 6 (b), (d) and (f)) indicate that CDRX

mechanism is more easily triggered at the low temperature (1000 ˚C), high strain rate (1.0 s^{-1}) and medium true strain (peaked at 0.51). Moreover, the fractions of LAGBs are far bigger than that of MAGBs under the deformation conditions under which CDRX is prone to occur, as depicted in Figs. 6 (b), (d) and (f). This manifests that LAGBs are rapidly transformed to HAGBs even if when CDRX happens easily. Additionally, the fraction of MAGBs is always less than 5.7% under the testing conditions, as shown in Fig. 6. Therefore, it is concluded that DDRX is a dominant DRX mechanism in Inconel 740 superalloy, while CDRX is not an active one due to the negligible fraction of MAGBs.

4. Dynamic recrystallization mechanisms

4.1. Discontinuous dynamic recrystallization

For the Nickel-based superalloy with low SFE, such as Inconel 740 superalloy, DRV is retarded due to the dissociation reaction impeding the cross slip and climb of dislocations [34]. Therefore, DDRX is initiated after reaching a critical condition (ε_c or critical dislocation density), and this mechanism is featured by DRX grain nucleation and subsequent growth [35, 36].

4.1.1. Pre-existing grain boundary bulging nucleation

Fig. 7 (a) shows that the first layer of DRX grains is characterized by the typical necklace structures, which is involved in DDRX mechanism. At the beginning of deformation, the new grains generated by DDRX have the grain boundaries bulging characteristic. The fluctuating grain boundaries are caused by the deformation, resulting in the bulging and serration HAGBs as the actual nucleation sites of DRX grains. This is because the additional non-uniform strains during hot deformation are developed by the grain boundary sliding (GBS) along initial HAGBs [36], leading to the presence of dislocation gradients near these boundaries. The dislocation density difference across the pre-existing HAGBs is the driving force of grain boundary bulging. The large local misorientation value can be corresponded to the high geometrically necessary dislocation density [37, 38]. These bulging areas in the vicinities of initial HAGBs are usually accompanied by the high dislocation density highlighted in Fig. 7 (b). Therefore, the grain boundary bulging is the consequence of local imbalance of dislocation density near the grain boundary of adjacent coarse grains. Moreover, it is worth noting that the pre-existing HAGB bulging is occasionally accompanied by the strain-induced sub-boundary with LAGB [35, 39], as shown by the rectangle in Fig. 7 (a).

This grain in the bulging area can be rotated by GBS [29, 34, 40]. In this process, the strain-induced sub-boundary continuously absorbs the lattice dislocations and rapidly transforms into HAGB. The formation of new HAGBs in DDRX is an order of magnitude much faster than that in CDRX [36]. This bulge can end up as the first DRX grain, which can constitute the necklace-like new grains.

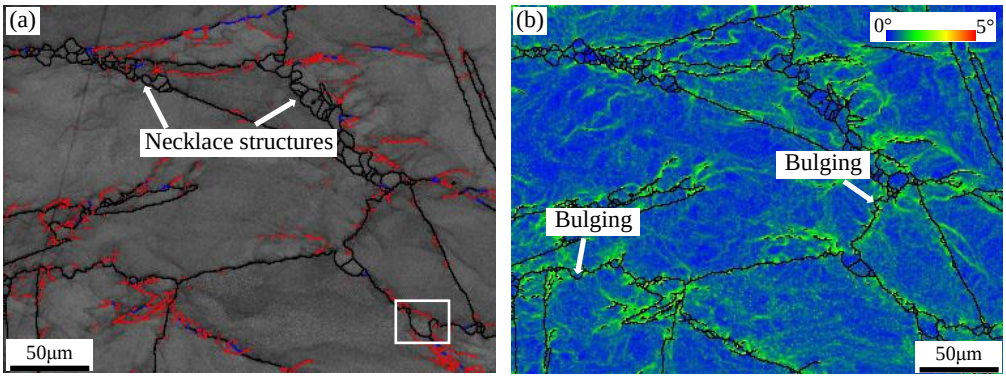

Fig.7. (a) The microstructure and (b) local misorientation map with LAGBs, MAGBs and HAGBs of Inconel 740 superalloy obtained at ε=0.36, $\dot{\varepsilon}$=0.1 s^{-1} and T=1100 ˚C.

4.1.2. Annealing twin assisting nucleation

Inconel 740 superalloy with low SFE, just as other Nickel-based superalloys, shows a strong tendency to form the annealing twins during DRX process. The driving force of twinning is caused by the migration of HAGBs [41]. The stacking error accumulation at some positions of migratory HAGB, results in the dissociation of this HAGB into the mobile incoherent twin segment and immobile coherent twin part as well as LAGB [40, 42]. This process can be regarded as a growth accident or a stacking error [20]. The twin boundaries can be continuously originated when this above process occurs repeatedly. In addition, the generation of twin boundaries is also depended on the interactions between the primary (Σ3) and the higher order twin boundaries (Σ9 and Σ27) [43], as follows: Σ3+Σ9→Σ3, Σ3+Σ9→Σ27 and Σ3+Σ3→Σ9. The interactions of Σ3 and Σ9 boundaries create new Σ3 and/or Σ27 boundaries. Moreover, the meeting of Σ3 boundaries generates new Σ9 boundaries. Σ3, Σ9 and Σ27 boundaries are detected through coincident site lattice (CSL) model in EBSD. The interactions of twin boundaries are found in A and B rectangle regions, as shown in Figs. 8 (a). However, it is found that most of twin boundaries have Σ3 (including coherent and incoherent) characteristic, as shown in Figs. 8 (a) and (b). Therefore, like other Nickel-based superalloys [11, 16], these interactions occur occasionally. Furthermore, the grain growth

direction approximates the normal direction of immobile coherent twin plane, and is deduced via the migrating boundary curvature [42], as shown by the red arrows in Fig. 8 (a). It well explains why to form the parallel twin boundaries within some DRX grain interiors.

Fig. 8 (b) reveals that the initial twin boundary loses its twin nature and is transformed into the usual HAGB due to the initial grain orientation change. Furthermore, the large majority of regenerated twin boundaries are located inside the necklace-like new grains, suggesting that the twinning occurred at the growth stage of DRX grains. Meanwhile, some new twin boundaries are also formed between DRX grain and initial grain, as shown by the rectangle in Fig. 8 (b). The local misorientations of straight coherent twin boundaries in DRX grain interiors are less than that of adjacent initial grain interiors, as highlighted in Fig. 8 (c). The twinning is regerded as an accommodation mechanism of grain boundary migration and dislocation slip [44]. The dislocation slip across these immobile coherent boundaries of low interfacial energy is difficult [33]. Therefore, DRX grain boundaries continuously bulge toward to the high dislocation density area of adjacent initial grains. Moreover, from Fig. 8 (c), the mobile twin boundaries behind the initial bulging areas can migrate to the adjacent high dislocation density area. In this process, the twin nature is losing, as shown by the rectangle in Fig. 8 (b), and these boundaries eventually are transformed into HAGBs. Therefore, the regenerated twin boundaries (Σ3) can accelerate the nucleation and growth process of DRX grains in DDRX. The origination of twin boundaries can be promoted by the faster mobility of grain boundaries on account of the higher deformation temperature [13].

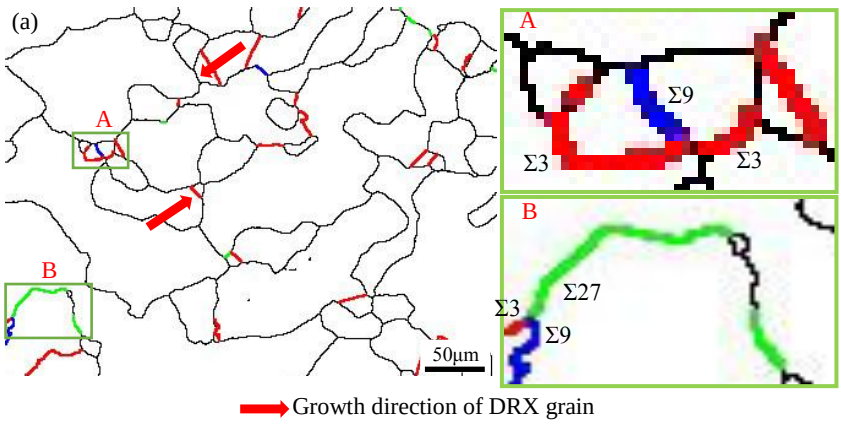

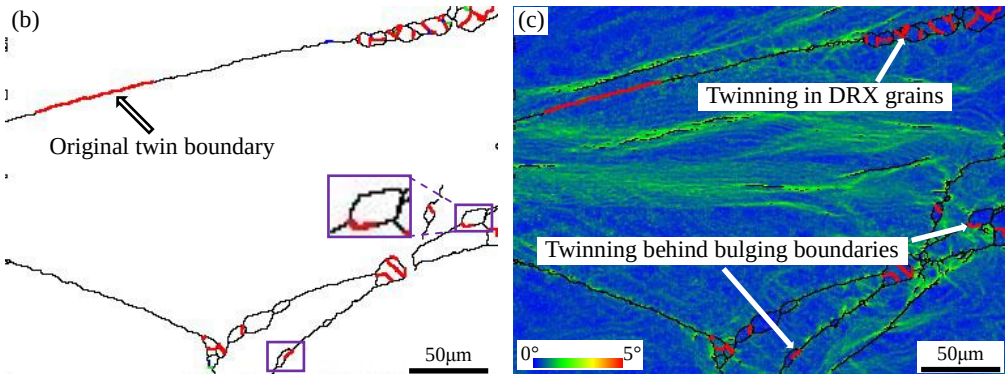

Fig.8. (a) Grain boundary map obtained at ε=0.8, $\dot{\varepsilon}$=0.01 s^{-1} and T=1200 ˚C; (b) Grain boundary map obtained at ε=0.36, $\dot{\varepsilon}$=1.0 s^{-1} and T=1100 ˚C and (c) local misorientation map of Inconel 740 superalloy corresponding to (b). (color code: (a) and (b) HAGBs-black, Σ27-green, Σ9-blue and Σ3-red; (c) LAGBs, MAGBs, HAGBs-black and Σ3-red).

4.2. Continuous dynamic recrystallization

CDRX accompanied by DRV [45], is considered as a continuous and slow process. In this process, the sub-boundaries (LAGBs) absorb continuously dislocations and transform eventually into HAGBs and new grains [16, 18]. There are not the recognizable nucleation and growth process involved in DRX grains from CDRX [35]. As the previous analysis, CDRX mechanism is easily developed by the low deformation temperatures and high strain rate.

4.2.1. Progressive subgrain rotation near pre-existing grain boundary

In Nickel-based superalloy, it is widely recognized that the partial DRX grains are originated from the progressive subgrain rotation based on the analysis of increasing cumulative misorientations near pre-existing HAGBs and across grain interiors [16, 19, 33]. Fig. 9 (a) represents abundant LAGBs at the initial boundaries and triple junctions. The dislocation tangles induced by strain are existed in these regions, as highlighted in Fig. 9 (b), indicating the high dislocation density. The coarsening subgrains with LAGBs are formed by the annihilation and rearrangement of dislocations [46], as shown in Fig. 9 (a). These subgrains can be called the strain-induced subgrians [47]. It is clearly observed that the strain-induced sub-boundaries are transformed into new HAGBs through the MAGBs transition near the pre-existing HAGBs, as shown by the rectangle in Fig. 9 (a). In other words, the subgrain with LAGBs near the pre-existing HAGBs, is transformed into a DRX grain with HAGBs by the progressive rotation, indicating the occurrence of CDRX. However, the progressive

rotation of subgrain occurs infrequently in the original grains under the testing conditions.

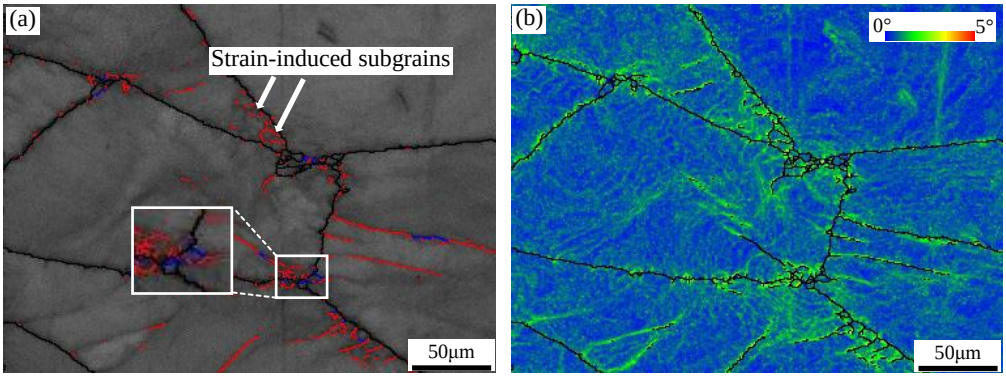

Fig.9. (a) The microstructure and (b) local misorientation map with LAGBs, MAGBs and HAGBs of Inconel 740 superalloy obtained at ε=0.36, $\dot{\varepsilon}$=0.01 s^{-1} and T=1000 ˚C.

4.2.2. Homogeneous misorientation increase in deformed grain

Fig. 10 (a) describes some regenerated HAGBs appear in the original grain interiors. The formation of these regenerated HAGBs, which seem not be related to the original HAGBs, is as a typical characteristic of CDRX [35]. The new HAGBs within interiors of deformed grains were also observed in other Nickel-based superalloys [16, 20, 28, 39, 48], while such a phenomenon had not been further explained. From Fig. 10 (a), it is noteworthy that these regenerated HAGBs can be formed along the shear direction inside the coarse deformed grains. Hence, these regenerated HAGBs can be called strain-induced HAGBs. The arrangement of dislocation substructures is expressed by dense dislocation walls (DDWs) in high dislocation density region. When DDWs are on the primary slip planes along the shear direction, the mobile dislocations are trapped into DDWs, resulting in the formation of LAGBs along the shear direction, as shown in Fig. 10 (b). LAGBs aligned along the shear direction are more liable to increase the misorientation at the low to medium strain [49]. Therefore, via MAGBs stage, the strain-induced HAGBs are generated by the increasing misorientation into LAGBs on the shear direction once the misorientation reaches a critical angle (15º). Such a phenomenon involved in the formation of strain-induced HAGBs is also observed in Figs. 7 (a) and 9 (a) (MAGBs stage), which implies that it is not accidental. It is believed that the high dislocation density (local misorientation value) is developed at the low deformation temperature, high strain rate and low to middle strain, since the average value of local misorientation angles, i.e., the level of dislocation density, is an inverse ratio with the fraction of DRX grains with dislocation-free [50]. The mechanism of these strain-induced

HAGBs formation is considered as the homogeneous misorientation increase in the deformed grains according to Huang's definition rule [35]. The strain-induced HAGBs in CDRX can be as a transitional stage for the formation of new grains because no DRX grains are formed in this process. It is found that the subgrains with LAGBs is formed in the vicinities of these HAGBs, moreover, the bulging of strain-induced HAGBs also be observed in Fig. 10 (a). Therefore, these new strain-induced HAGBs in the deformed grains can be involved in the above DDRX and the progressive subgrain rotation near HAGBs in CDRX.

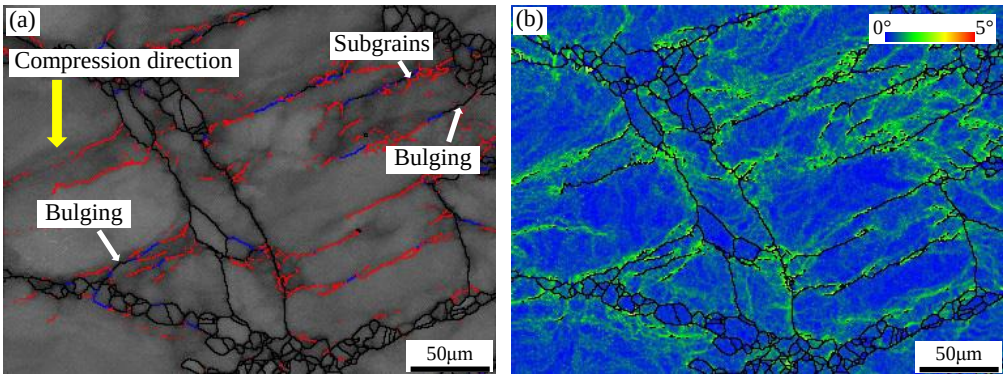

Fig.10. (a)The microstructure and (b) local misorientation map with LAGBs, MAGBs and HAGBs of Inconel 740 superalloy obtained at ε=0.51, $\dot{\varepsilon}$=0.1 s^{-1} and T=1100 ˚C.

4.3. Mixed dynamic recrystallization mechanism

For Inconel 740 superalloy, Fig. 11 depicts the mixed DRX mechanisms involving DDRX in Fig. 11 (a) and CDRX in Figs. 11 (b) and (c) during hot deformation. In DDRX, the difference in dislocation density between adjacent initial grains is caused by GBS, resulting in the local migration of the original HAGBs. Fig. 11 (a) describes that a portion of HAGB is moved towards the region of high dislocation density, indicating the appearance of pre-existing HAGB bulging. The dislocation behind this bulging part is accumulated towards a critical dislocation density of initiating DRX [35, 51], meanwhile, the accumulation of dislocation is also used for harmonizing the plastic deformation [52]. As the strain is increased, this bulging area can be isolated by the sub-boundary resulting from the dislocation accumulation. Finally, this sub-boundary is transformed into a new HAGB through continuously absorbing lattice dislocations. Besides, the nucleation of DRX grains is also promoted by twinning behind the bulged HAGBs, while the formation of Σ3 boundaries in DRX grains is beneficial for growth of DRX grains. On the other hand, the strain-induced sub-boundary behind the bulge of initial HAGB in the rectangle of Fig. 7 (a) is formed at the

low deformation temperature and high strain rate. This sub-boundary contributes to a new grain nucleus during subsequent hot deformation [29, 34, 35].

Fig. 11 (b) represents the progressive subgrain rotation near the pre-existing boundary. When the strain is low, the cross-slip of dislocations can be more activated in the vicinities of pre-existing HAGBs owing to the stress concentration [53], leading to the appearance of dislocation cells. With the increasing strain, the polygonized subgrains with LAGBs are developed by the dislocation rearrangement near original HAGBs. The progressive subgrain rotation occurs in subsequent hot deformation, where these subgrains with LAGBs are transformed into DRX grains with HAGBs via MAGBs stage. Moreover, one reason of subgrain rotation considers the difference between the energies of two adjacent LAGBs [54]. The rotation occurs because the energy increase of a LAGB is lower than the decrease in energy of the other LAGB, indicating the rotation promoted by a total decrease in boundary energy. The other rotation reason is concerned with the subgrain near the bulging and serrated initial HAGBs at the early deformation [32, 55]. GBS can still act on the bulging part of HAGB during subsequent deformation, while the remaining part has to adapt the strain via the plastic deformation. Therefore, the occurrence of subgrain rotation beside this HAGB results from the asymmetric modality of this boundary.

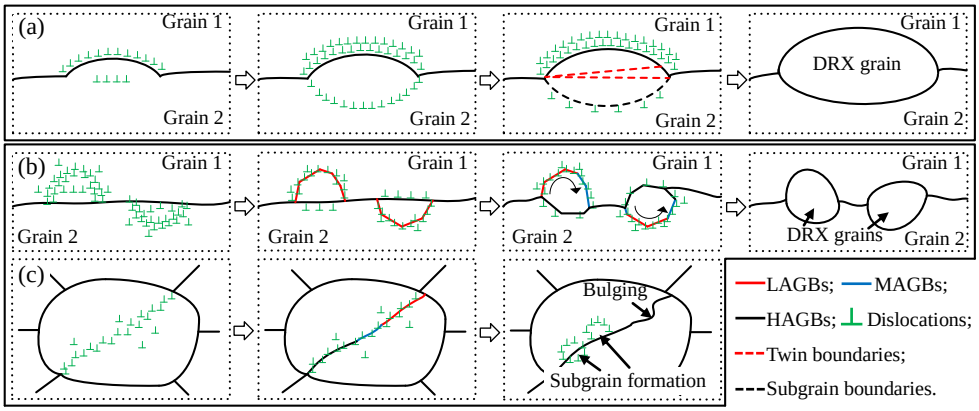

Fig. 11. Schematic illustration of the mixed dynamic recrystallization mechanisms: (a) the process of DDRX; (b) and (c) the processes of CDRX.

Fig. 11 (c) shows that the homogeneous misorientation increase inside the deformed grains is considered as the other CDRX mechanism. Through the MAGB stage, LAGB absorbs continuously the lattice dislocations, resulting in the formation of a new HAGB along the

shear direction in the deformed grain interior. Based on Section 4.2.2, it is emphasized that the new HAGB is eventually involved in the mechanisms of Figs. 11 (a) and (b) during subsequent hot deformation due to the appearance of bulging and subgrains on it.

5. Conclusions

The microstructures of Inconel 740 superalloy were investigated by the well-designed isothermal compression tests. Different DRX mechanisms involved in DDRX and CDRX were analyzed and a mixed DRX mechanism was proposed and validated via the observation of the DRX process. The primary conclusions in this work are listed as follows:

(1) The critical strains of DRX initiation at the deformation temperatures of 1000-1200 ˚C and strain rates of 0.1-1.0 s^{-1} are determined. The function relationship of critical strain and peak strain is identified as $\varepsilon_c=0.6\varepsilon_p$.

(2) The size and volume fraction of DRX grains are increased through the increasing deformation temperature and decreasing strain rate. DDRX covering the original HAGBs bulging nucleation and the twinning assisting nucleation, and CDRX involving the progressive subgrain rotation near the initial HAGBs and the homogeneous misorientation increase in the deformed grains contribute simultaneously to the mixed DRX mechanism during hot deformation. But DDRX plays a dominant role. CDRX is more developed at the low deformation temperature (1000 ˚C), high strain rate (1.0 s^{-1}) and medium strain (0.51).

(3) The strain-induced HAGBs resulting from the homogeneous misorientation increase within the deformed grains tend to form along the shear direction. These new HAGBs are finally involved in DDRX and the progressive subgrain rotation near HAGBs in CDRX.

(4) The high local misorientation associated with the high dislocation density area is located near LAGBs and the bulging HAGBs, which becomes the potential nucleation sites for DRX grains via DDRX and CDRX mechanisms.

Acknowledgements

Authors acknowledge the funding supported by National Natural Science Foundation of

China (No. 51575039), NSAF (No. U1730121) and the Joint fund (general) fund project of the Ministry of Education (No. 6141A020221)

References

[1] R. Viswanathan, J. F. Henry, J. Tanzosh, G. Stanko, J. Shingledecker, B. Vitalis, R. Purgert, U. S. program on materials technology for ultra-supercritical coal power plants, J. Mater. Eng. Perform. 14 (2005) 281-292.

[2] N. N. Aung, X. Liu, Effect of temperature on coal ash hot corrosion resistance of Inconel 740 superalloy, Corros. Sci. 82 (2014) 227-238.

[3] M. Abbasi, D. I. Kim, J. H. Shim, W. S. Jung, Effects of alloyed aluminum and titanium on the oxidation behavior of INCONEL 740 superalloy, J. Alloys Compd. 658 (2016) 210-221.

[4] G. S. Shin, J. Y. Yun, M. C. Park, S. J. Kim, Effect of Mo on the thermal stability of γ′ precipitate in Inconel 740 alloy, Mater. Charact. 95 (2014) 180-186.

[5] J. P. Shingledecker, N. D. Evans, G. M. Pharr, Influences of composition and grain size on creep-rupture behavior of Inconel® alloy 740, Mater. Sci. Eng. A 578 (2013) 277-286.

[6] N. D. Evans, P. J. Maziasz, R. W. Swindeman, G. D. Smith, Microstructure and phase stability in INCONEL alloy 740 during creep, Scripta Mater. 51 (2004) 503-507.

[7] X. You, Y. Tan, Q. You, S. Shi, J. Li, F. Ye, X. Wei, Preparation of Inconel 740 superalloy by electron beam smelting, J. Alloys Compd. 676 (2016) 202-208.

[8] C. Sun, G. Liu, Q. Zhang, R. Li, L. Wang, Determination of hot deformation behavior and processing maps of IN 028 alloy using isothermal hot compression test, Mater. Sci. Eng. A 595 (2014) 92-98.

[9] Y. C. Lin, X. M. Chen, A critical review of experimental results and constitutive descriptions for metals and alloys in hot working, Mater. Des. 32 (2011) 1733-1759.

[10] Q. Guo, D. Li, S. Guo, H. Peng, J. Hu, The effect of deformation temperature on the microstructure evolution of Inconel 625 superalloy, J. Nucl. Mater. 414 (2011) 440-450.

[11] H. Jiang, J. Dong, M. Zhang, Z. Yao, Evolution of twins and substructures during low strain rate hot deformation and contribution to dynamic recrystallization in alloy 617B, Mater. Sci. Eng. A 649 (2016) 369-381.

[12] H. Jiang, J. Dong, M. Zhang, Z. Yao, Phenomenological model for the effect of strain rate on recrystallization and grain growth kinetics in the 617B alloy, J. Alloys Compd. 735 (2018) 1520-1535.

[13] H. Zhang, H. Zhou, S. Qin, J. Liu, X. Xu, Effect of deformation parameters on twinning evolution during hot deformation in a typical nickel-based superalloy, Mater. Sci. Eng. A 696 (2017) 290-298.

[14] Y. Wang, W. Z. Shao, L. Zhen, L. Yang, X. M. Zhang, Flow behavior and microstructures of superalloy 718 during high temperature deformation, Mater. Sci. Eng. A 497 (2008) 479-486.

[15] Z. Wan, L. Hu, Y. Su, T. Wang, Z. Li, Microstructure evolution and dynamic softening mechanisms during high-temperature deformation of a precipitate hardening Ni-based superalloy, Vacuum 155 (2018) 585-593.

[16] H. Zhang, K. Zhang, S. Jiang, H. Zhou, C. Zhao, X. Yang, Dynamic recrystallization behavior of a γ'-hardened nickel-based superalloy during hot deformation, J. Alloys Compd. 623 (2015) 374-385.

[17] Y. C. Lin, D. G. He, M. S. Chen, X. M. Chen, C. Y. Zhao, X. M, Z. L. Long, EBSD analysis of evolution of dynamic recrystallization grains and δ phase in a nickel-based superalloy during hot compressive deformation, Mater. Des. 97 (2016) 13-24.

[18] Y. Liu, Y. Ning, Z. Yao, H. Li, X. Miao, Y. Li, Z. Zhao, Plastic deformation and dynamic recrystallization of a powder metallurgical nickel-based superalloy, J. Alloys Compd. 675 (2016) 73-80.

[19] Y. C. Lin, X. Y. Wu, X. M. Chen, J. Chen, D. X. Wen, J. L. Zhang, L. T. Li, EBSD study of a hot deformed nickel-based superalloy, J. Alloys Compd. 640 (2015) 101-113.

[20] M. Azarbarmas, M. Aghaie-Khafri, J. M. Cabrera, J. Calvo, Dynamic recrystallization mechanisms and twining evolution during hot deformation of Inconel 718, Mater. Sci. Eng. A 678 (2016) 137-152.

[21] S. Gourdet, F. Montheillet, An experimental study of the recrystallization mechanism during hot deformation of aluminium, Mater. Sci. Eng. A 283 (2000) 274-288.

[22] N. D. Ryan, H. J. McQueen, Flow stress, dynamic restoration, strain hardening and ductility in hot working of 316 steel, J. Mater. Process. Technol. 21 (1990) 177-199.

[23] C. Zhang, L. Zhang, W. Shen, Q. Xu, Y. Cui, The processing map and microstructure evolution of Ni-Cr-Mo-based C276 superalloy during hot compression, J. Alloys Compd. 728 (2017) 1269-1278.

[24] M. Wang, W. Wang, Z. Liu, C. Sun, L. Qian, Hot workability intergrating processing and activation energy maps of Inconel 740 superalloy, Mater. Today Commun. 14 (2018) 188-198.

[25] A. Belyakov, T. Sakai, H. Miura, K. Tsuzaki, Grain refinement in copper under large strain deformation, Philos. Mag. A 81 (2001) 2629-2643.

[26] D. X. Wen, Y. C. Lin, H. B. Li, X. M. Chen, J. Deng, L. T. Li, Hot deformation behavior and processing map of a typical nickel-based superalloy, Mater. Sci. Eng. A 591 (2014) 183-192.

[27] D. Feng, X. M. Zhang, S. D. Liu, Y. L. Deng, Constitutive equation and hot deformation behavior of homogenized Al-7.68Zn-2.12Mg-1.98Cu-0.12Zr alloy during compression at elevated temperature, Mater. Sci. Eng. A 608 (2014) 63-72.

[28] D. Li, Q. Guo, S. Guo, H. Peng, Z. Wu, The microstructure evolution and nucleation mechanism of dynamic recrystallization in hot-deformed Inconel 625 superalloy, Mater. Des. 32 (2011) 696-705.

[29] A. M. Wusatowska-Sarnek, H. Miura, T. Sakai, Nucleation and microtexture development under dynamic recrystallization of copper, Mater. Sci. Eng. A 323 (2002) 177-186.

[30] S. S. S. Kumar, T. Raghu, P. P. Bhattacharjee, G. A. Rao, U. Borah, Work hardening characteristics and microstructural evolution during hot deformation of a nickel superalloy at moderate strain rates, J. Alloys Compd. 709 (2017) 394-409.

[31] J. Fu, F. Li, J. Sun, Y. Wu, Texture, orientation, and mechanical properties of Ti-stabilized Fe-17Cr ferritic stainless steel, Mater. Sci. Eng. A 738 (2018) 335-343.

[32] X. Yang, H. Miura, T. Sakai, Continuous Dynamic Recrystallization in a Superplastic 7075 Aluminum Alloy, Mater. Trans. 10 (2002) 2400-2407.

[33] S. S. S. Kumar, T. Raghu, P. P. Bhattacharjee, G. A. Rao, U. Borah, Strain rate dependent microstructural evolution during hot deformation of a hot isostatically processed nickel base superalloy, J. Alloys Compd. 681 (2016) 28-42.

[34] T. Sakai, J. J. Jonas, Plastic Deformation: Role of Recovery and Recrystallization, Reference Module in Materials Science and Materials Engineering, Elsevier, Oxford, 2016.

[35] K. Huang, R. E. Logé, A review of dynamic recrystallization phenomena in metallic materials, Mater. Des. 111 (2016) 548-574.

[36] T. Sakai, A. Belyakov, R. Kaibyshev, H. Miura, J.J. Jonas, Dynamic and post-dynamic recrystallization under hot, cold and severe plastic deformation conditions, Prog. Mater. Sci. 60 (2014) 130-207.

[37] J. McCarley, S. Tin, Utilization of hot deformation to trigger strain induced boundary

migration (SIBM) in Ni-base superalloys, Mater. Sci. Eng. A 720 (2018) 189-202.

[38] K. Wang, X. Li, Q. Li, G. Shu, G. Tang, Hot deformation behavior and microstructural evolution of particulate-reinforced AA6061/B4C composite during compression at elevated temperature, Mater. Sci. Eng. A 696 (2017) 248-256.

[39] M. Zouari, N. Bozzolo, R. E. Loge, Mean field modelling of dynamic and post-dynamic recrystallization during hot deformation of Inconel 718 in the absence of δ phase particles, Mater. Sci. Eng. A 655 (2016) 408-424.

[40] Y. Wang, W. Z. Shao, L. Zhen, X. M. Zhang, Microstructure evolution during dynamic recrystallization of hot deformed superalloy 718, Mater. Sci. Eng. A486 (2008) 321-332.

[41] N. Bozzolo, N. Souaï, R. E. Logé, Evolution of microstructure and twin density during thermomechanical processing in a γ-γ' nickel-based superalloy, Acta Mater. 60 (2012) 5056-5066.

[42] S. Mahajan, C.S. Pande, M.A. Imam, B.B. Rath, Formation of annealing twins in f.c.c. crystals, Acta Mater. 45 (1997) 2633-2638.

[43] T. S. Prithiv, P. Bhuyan, S. K. Pradhan, V. S. Sarma, S. Mandal, A critical evaluation on efficacy of recrystallization vs. strain induced boundary migration in achieving grain boundary engineered microstructure in a Ni-base superalloy, Acta Mater. 146 (2018) 187-201.

[44] W. Wang, S. Lartigue-Korinek, F. Brisset, A. L. Helbert, J. Bourgon, T. Baudin, Formation of annealing twins during primary recrystallization of two low stacking fault energy Ni-based alloys, J. Mater. Sci, 50 (2015) 2167-2177.

[45] C. Poletti, L. Germain, F. Warchomicka, M. Dikovits, S. Mitsche, Unified description of the softening behavior of beta-metastable and alpha+beta titanium alloys during hot deformation, Mater. Sci. Eng. A 651 (2016) 280-290.

[46] F. J. Humphreys, M. Hatherly, Recrystallization and related annealing phenomena, 2nd ed. Elsevier, Oxford, 2004.

[47] N. Dudova, A. Belyakov, T. Sakai, R. Kaibyshev, Dynamic recrystallization mechanisms operating in a Ni-20%Cr alloy under hot-to-warm working, Acta Mater. 58 (2010) 3624-3632.

[48] H. Zhang, K. Zhang, H. Zhou, Z. Lu, C. Zhao, X. Yang, Effect of strain rate on microstructure evolution of a nickel-based superalloy during hot deformation, Mater. Des. 80 (2015) 51-62.

[49] R. Kaibyshev, K. Shipilova, F. Musin, Y. Motohashi, Continuous dynamic

recrystallization in an Al-Li-Mg-Sc alloy during equal-channel angular extrusion, Mater. Sci. Eng. A 396 (2005) 341-351.

[50] Y. Cao, H. Di, Research on the hot deformation behavior of a Fe-Ni-Cr alloy (800H) at temperatures above 1000 ˚C, J. Nucl. Mater. 465 (2015) 104-115.

[51] J. Qu, X. Xie, Z. Bi, J. Du, M. Zhang, Hot deformation characteristics and dynamic recrystallization mechanism of GH4730 Ni-based superalloy, J. Alloys Compd. 785 (2019) 918-924.

[52] Y. Wu, M. Zhang, X. Xie, F. Lin, S. Zhao, Dynamic recrystallization of a new nickel-based alloy for 700 °C A-USC power plant applications with different initial states: as-homogenized and as-forged, J. Alloys Compd. 662 (2016) 283-295.

[53] A. Galiyev, R. Kaibyshev, G. Gottstein, Correlation of plastic deformation and dynamic recrystallization in magnesium alloy AK60, Acta Mater. 49 (2001) 1199-1207.

[54] H. Hu, Direct observations on the annealing of Si-Fe crystals in the electron microscope, Trans. Metall. Soc. A. I. M. E. 224 (1962) 75-84.

[55] M. R. Drury, F. J. Humphreys, The development of microstructure in Al-5% Mg during high temperature deformation, Acta Metall. 34 (1986) 2259-2271.

Figure captions

Fig.1. Initial state of Inconel 740 superalloy: (a) optical microscope and (b) distribution of misorientation angle.

Fig.2. DRX behavior of Inconel 740 superalloy: (a) flow curve and a relationship between θ and σ obtained at T=1200 ˚C and $\dot{\varepsilon}$=0.01 s^{-1}; (b) ε_c values at different deformation conditions.

Fig.3. The microstructure of Inconel 740 superalloy obtained at ε=0.51 and $\dot{\varepsilon}$=0.01 s^{-1} with a deformation temperature of: (a) 1000 ˚C; (b) 1100 ˚C and (c) 1200 ˚C. (color code: black-HAGBs, blue-MAGBs and red-LAGBs).

Fig.4. The microstructure of Inconel 740 superalloy obtained at ε=0.8 and T=1100 ˚C with a strain rate of: (a) 0.01 s^{-1}; (b) 0.1 s^{-1} and (c) 1.0 s^{-1}.

Fig.5. Variations of misorientation gradient measured along A-F lines marked in Figs. 3 and 4.

Fig.6. Distributions of misorientation angle of Inconel 740 superalloy obtained at: (a) at $\dot{\varepsilon}$ =0.01 s^{-1} and ε=0.51 with different deformation temperatures of 1000, 1100 and 1200 ˚C; (c) T=1100 ˚C and ε=0.8 with different strain rates of 0.01, 0.1 and 1.0 s^{-1}; (e) T=1100 ˚C and $\dot{\varepsilon}$ =0.1 s^{-1} with different true strains of 0.22, 0.36, 0.51 and 0.8. (b), (d) and (f) corresponding to the fractions of LAGBs, MAGBs and HAGBs in (a), (c) and (e), respectively.

Fig.7. (a) The microstructure and (b) local misorientation map with LAGBs, MAGBs and HAGBs of Inconel 740 superalloy obtained at ε=0.36, $\dot{\varepsilon}$=0.1 s^{-1} and T=1100 ˚C.

Fig.8. (a) Grain boundary map obtained at ε=0.8, $\dot{\varepsilon}$=0.01 s^{-1} and T=1200 ˚C; (b) Grain boundary map obtained at ε=0.36, $\dot{\varepsilon}$=1.0 s^{-1} and T=1100 ˚C and (c) local misorientation map of Inconel 740 superalloy corresponding to (b). (color code: (a) and (b) HAGBs-black, Σ27-green, Σ9-blue and Σ3-red; (c) LAGBs, MAGBs, HAGBs-black and Σ3-red).

Fig.9. (a) The microstructure and (b) local misorientation map with LAGBs, MAGBs and HAGBs of Inconel 740 superalloy obtained at ε=0.36, $\dot{\varepsilon}$=0.01 s^{-1} and T=1000 ˚C.

Fig.10. (a)The microstructure and (b) local misorientation map with LAGBs, MAGBs and HAGBs of Inconel 740 superalloy obtained at ε=0.51, $\dot{\varepsilon}$=0.1 s^{-1} and T=1100 ˚C.

Fig. 11. Schematic illustration of the mixed dynamic recrystallization mechanisms: (a) the process of DDRX; (b) and (c) the processes of CDRX.